Self-guided navigation of magnetic microspheres on topographic landscapes

Yiyang Wu,[†] April Ramos,[‡] and Kyle J. M. Bishop[*,†]

[†]*Department of Chemical Engineering, Columbia University, New York, NY 10027 USA*

[‡]*Department of Chemistry, Barnard College, New York, NY, 10027 USA*

E-mail: kyle.bishop@columbia.edu

Abstract

The directed propulsion of magnetic microrobots through structured environments often requires real-time feedback between external sensors and the applied field. This requirement, however, can be relaxed to enable self-guided propulsion by coupling field-driven motion to gradients in the local environment. We show that rotating fields direct the migration of ferromagnetic spheres up local gradients in the topography of a solid substrate. We quantify the speed and direction of particle migration as a function of rotation frequency and incline angle. These observations are explained by a dynamical model that describes particle motion through the fluid due to the magnetic torque and gravitational force. We demonstrate how "topotaxis" can direct the simultaneous navigation of multiple particles on patterned arrays of concave bowls and convex domes without knowledge of the particle locations or the surface topography. These results highlight opportunities for designing time-varying fields to achieve other self-guided behaviors conditioned on local environmental cues.

Keywords

colloids, microrobot, autonomous, hydrodynamics, field-driven

Introduction

The remote actuation of magnetic particles by time-varying fields provides a basis for powering the dynamic functions[1] of microrobots[2] on the scale of living cells. These magnetic microrobots can navigate fluid environments by swimming[3–6] or surface rolling,[7–9] capture and release cargo through tunable deformations,[10–12] and apply precise stresses that alter their surroundings.[13–15] Owing to their small size, individual particles can fit through narrow constrictions of structured environments and later assemble to form functional swarms of many interacting robots.[16–18] These and other capabilities are motivated by emerging applications in biomedicine, where microrobots promise minimally-invasive solutions for targeted delivery and microsurgery.[19–23] In this context, magnetic fields provide an attractive power source due to their biocompatibility, minimal interaction with biological tissues, and dynamically tunable magnitude and direction. However, such fields are "blunt instruments" that act uniformly over large volumes containing many microrobots, which creates challenges for controlling individual particles in heterogeneous environments.

The external control of magnetic microrobots often relies on real-time monitoring of particle positions and continuous adjustment of the applied field to achieve desired behaviors.[24,25] For a single particle, such feedback control algorithms tune multiple electromagnets to direct particle motion along specified trajectories in two or three dimensions.[26] When, however, the position of the particle and/or the targeted location are unknown, these methods become ineffective. Moreover, external control systems based on magnetic fields are not easily extended to direct the behaviors of multiple particles independently due to their limited spatial resolution. To first approximation, neighboring particles move under the influence of a common field. These challenges of limited information and global actuation motivate

the development of self-guided microrobots that rely on local environmental cues to determine their appropriate behaviors. Active particles[27] that direct self-propelled motions in response to local gradients—for example, in solute concentration,[28,29] fluid velocity,[30,31] and light intensity[32,33]—provide canonical examples of such self-guided capabilities. However, it remains an outstanding challenge to combine the benefits of magnetic actuation with the autonomy of gradient-driven 'taxis'.

Recent work suggests that time-varying magnetic fields can be used to encode the self-guided behaviors of magnetic particles conditioned on local environmental cues.[34,35] For example, Dou et al. identify spatially homogeneous, time-periodic fields that direct the migration of ferromagnetic spheres up (or down) an inclined plane—so-called topotaxis.[34] Owing to their rotational symmetry, such fields do not specify which direction the particle should move but rather how it should respond to local variations in the surface topography. Consequently, the same field can drive multiple independent particles to move simultaneously in different directions determined by their respective environments. These prior results are based on mathematical models of the particle dynamics and require complex time-periodic fields to direct uphill migration. Preliminary experiments provide evidence of topotaxis on *simulated* inclines achieved by tilting the axis of the applied field above a planar substrate. By contrast, self-guided particle migration on topographic landscapes and against the force of gravity has yet to be demonstrated.

Here, we present experimental evidence that simple rotating fields can direct topotaxis of ferromagnetic spheres up inclined substrates. We quantify the particle velocity along directions parallel and perpendicular to an inclined plane as a function of the rotation frequency and the incline angle. Consistent with theoretical predictions, the velocity perpendicular to the incline increases linearly with frequency while that parallel to the incline increases quadratically. By toggling the sign of the rotation frequency, motion perpendicular to the incline can be eliminated. At sufficiently high frequencies, we show that such toggled fields can direct particle migration up the incline against the force of gravity. Beyond planar

substrates, we demonstrate self-guided particle migration across curved topographies such as concave bowls and convex domes. Perhaps most importantly, we confirm experimentally that multiple (non-interacting) particles subject to a common field migrate independently along different directions as directed by their local environments. We discuss the limits and possible extensions of field-driven taxis in pursuit of magnetic microrobots with increasing levels of autonomy.

Results & Discussion

Toggled rotating fields drive "zig-zag" particle trajectories on inclined substrates

Our experiments are based on magnetic Janus spheres (radius $a = 5$ μm) dispersed in water above a planar substrate (Fig. 1a). As detailed in the Methods, the particles are prepared by depositing a thin nickel film onto a monolayer of polystyrene (PS) spheres. As established in prior studies,[36–38] the resulting particles are characterized by a permanent magnetic moment $\mathbf{m}$ directed parallel to the Janus equator with a magnitude $m \approx 1 \times 10^{-12}$ A m^2 that depends on the particle size and the nickel layer thickness. This approach offers ferromagnetic particles of tunable size and magnetization; however, the Janus character of the particles is not otherwise important to our present results.

The ferromagnetic particles are subject to a rotating field with magnitude B and angular frequency $\boldsymbol{\omega} = \omega \mathbf{e}_z$ aligned parallel to the gravity direction $\mathbf{g} = -g\mathbf{e}_z$. The sign of the rotation frequency ω is toggled periodically thereby reversing the direction of rotation after every 50 revolutions. When the substrate is level, particles are observed to rotate in place with little or no lateral translation due to gravity or the applied field. When, however, the substrate is tilted by a small angle α, particles migrate across the substrate along zig-zag trajectories, changing their direction of motion with each reversal of the rotating field. At low frequencies (e.g., $\omega = 10$ rad/s), particles follow zig-zag trajectories down the incline in the negative y-direction (Fig. 1b and movie S1). By contrast, at higher frequencies (e.g.,

$\omega = 70$ rad/s), particles zig-zag up the inline in the positive y-direction and against the force of gravity (Fig. 1c and movie S1).

Upon closer inspection of Figures 1b and c, we observe that the downhill migration velocity at low frequencies is not antiparallel to the uphill migration velocity at high frequencies. As detailed below and in the Supporting Information (Fig. S3), this observation is attributed to a small misalignment between the axis of the rotating field and the gravity direction. In principle, there are two "uphill" directions: (1) one based on the surface normal vector $\mathbf{n}$ and the gravity vector $\mathbf{g}$ (denoted $\mathbf{e}_y$ in Fig. 1a), and (2) another based on $\mathbf{n}$ and the angular frequency vector $\boldsymbol{\omega}$ (denoted $\mathbf{e}_2$ in Fig. 1c). The second uphill direction based on the rotating field will prove more useful in understanding the frequency-dependent migration of the particles. We therefore analyze the segments of each zig-zag trajectory to infer the average migration velocity of each particle along the $\mathbf{e}_1$ and $\mathbf{e}_2$ directions for different rotation frequencies and incline angles.

Velocity components U_1 and U_2 are odd and even functions of frequency

Figure 2 shows the components of the particle velocity perpendicular (U_1) and parallel (U_2) to the incline as a function of the rotation frequency. The velocity U_1 perpendicular to the uphill direction is well approximated by an odd function of frequency, which varies linearly with ω at small frequencies (Fig. 2a, solid markers). For positive frequencies (clockwise rotation viewed from below), the particle moves in the positive 1-direction. In other words, a particle navigating an inclined landscape moves to its right when facing the uphill direction. For negative frequencies, the particle moves in the opposite direction. When the incline angle is reduced or eliminated, the migration velocity is similarly reduced (Fig. 2a, open markers).

By contrast, the velocity U_2 parallel to the uphill direction is well approximated by an even function of frequency, which varies quadratically with ω at small frequencies (Fig. 2b, closed markers). In the limit as $\omega \to 0$, the particle sediments down the incline under the force of gravity. The rotating field introduces a second contribution directed up the incline

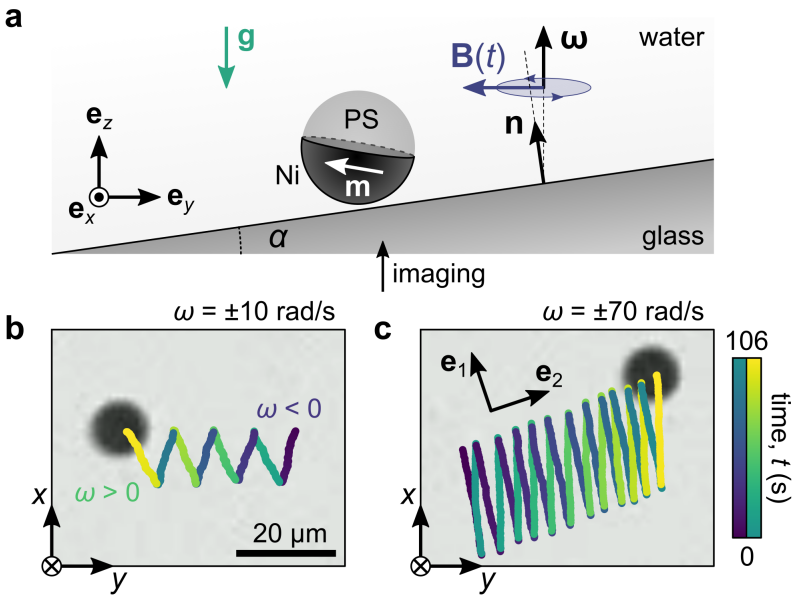

Figure 1: Topotaxis of a ferromagnetic sphere. (a) Schematic illustration of a Janus sphere with magnetic moment $\mathbf{m}$ moving on an inclined substrate due to a rotating field $\mathbf{B}(t)$. The angular frequency of the rotating field $\boldsymbol{\omega}$ is (approximately) parallel to the gravity direction $\mathbf{g}$ but tilted by an angle α from the surface normal vector $\mathbf{n}$. The frequency is toggled periodically between positive and negative values corresponding to clockwise and anticlockwise rotation as viewed from below. (b) At low frequencies (here, $\omega = \pm 10$ rad/s), the particle moves steadily down the incline (negative $\mathbf{e}_y$ direction) as it moves back and forth perpendicular to the incline ($\mathbf{e}_x$ direction). Colored markers denote the particle position at regular time intervals. (c) At high frequencies (here, $\omega = \pm 70$ rad/s), the particle zig-zags up the incline along the $\mathbf{e}_2$ direction, which differs slightly from the $\mathbf{e}_y$ direction. The incline angle in (b) and (c) is $\alpha = 16°$.

which increases as ω^2. At sufficiently high frequencies (e.g., ∼50 rad/s in Fig. 2b), this field-driven contribution exceeds that due to gravity thereby propelling particle migration up the inclined surface. The migration velocity is significantly reduced when the surface is nearly level with respect to the gravity direction and the rotation axis (Fig. 2b, open markers).

Dynamical models of topotaxis reproduce experimental observations

We developed a mathematical model of topotaxis based on low Reynolds number hydrodynamics that describes particle translation and rotation due to the external magnetic torque and the gravitational force.[34] As detailed in the Methods, we consider a solid sphere with a permanent magnetic moment $\mathbf{m}$ immersed in a viscous fluid above a solid plane (see also Supporting Information). The rotating field $\mathbf{B}(t)$ creates a magnetic torque $\mathbf{T}_\mathrm{m} = \mathbf{m} \times \mathbf{B}$ that acts to rotate the particle and align its moment parallel to the field. Due to hydrodynamic coupling between the sphere and plane, this time-periodic torque contributes also to particle translation parallel to the surface. We use multiple scale perturbation methods[39] to derive the components of the average migration velocity directed perpendicular (U_1) and parallel (U_2) to the incline

$$\frac{\langle U_1 \rangle}{a\omega_0} = \left(\frac{\kappa(1+\lambda)}{2\lambda} - \frac{\kappa^2(1+\lambda)}{2\lambda} G \right) \left(\frac{\omega}{\omega_0} \right) \alpha \tag{1}$$

$$\frac{\langle U_2 \rangle}{a\omega_0} = \left[-\left(\mu - \tfrac{1}{2}\kappa^2 \right) G + \left(\frac{\kappa(\lambda^2-1)}{2\lambda^2} - \frac{\kappa^2(1+\lambda)}{2\lambda} G \right) \left(\frac{\omega}{\omega_0} \right)^2 \right] \alpha \tag{2}$$

These equations are valid for small inclines α and small frequencies $\omega \ll \omega_0$, where $\omega_0 = mBY_c/6\pi\eta a^3$ is a characteristic relaxation rate for field driven rotation. The quantities $\mu = Y_a/Y_c$, $\kappa = Y_b/Y_c$, and $\lambda = X_c/Y_c$ are ratios between hydrodynamic mobility coefficients for a sphere rotating and translating above a plane (Fig. S1; e.g., $\mu = 0.86$, $\kappa = 0.071$, $\lambda = 1.45$, $Y_c = 0.45$ for a surface separation of $0.05a$).[40–43] The dimensionless parameter $G = Mga/mB$ describes the relative importance of the gravitational force and the magnetic torque, where M is the buoyant mass of the particle. Equations (1) and (2) further assume

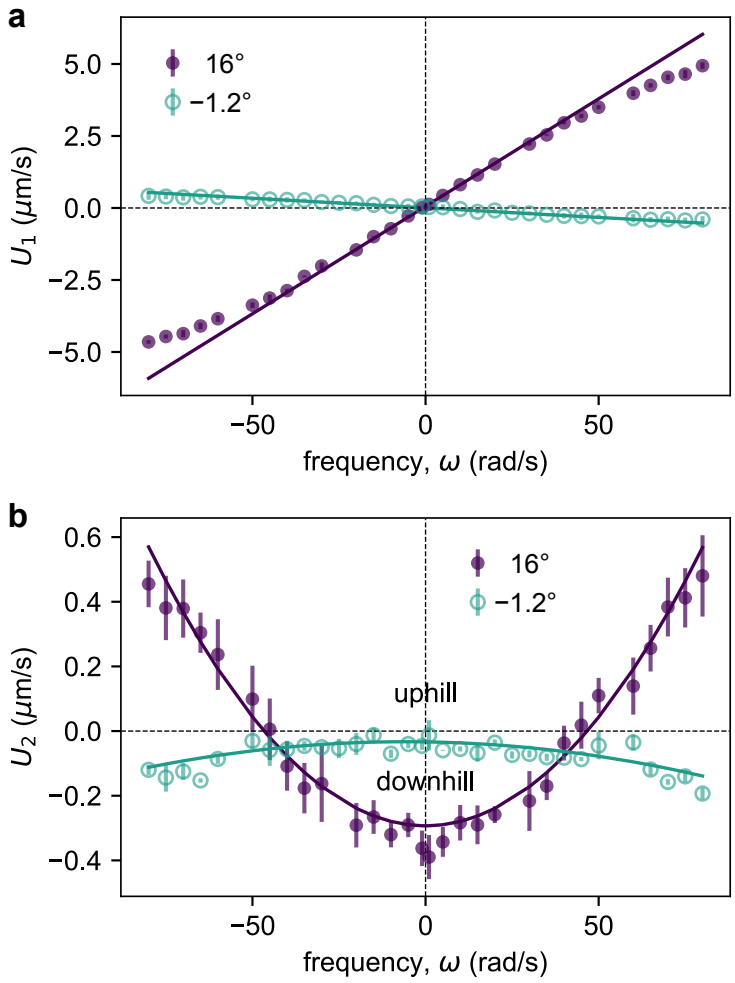

Figure 2: Individual particles moving on an inclined plane. (a) The average particle velocity perpendicular to the incline—denoted U_1—increases linearly with the frequency ω of the rotating field and the angle α of the incline. Markers denote data collected for an single particle at different frequencies for two incline angles $\alpha = 16°$ (filled circles) and $-1.2°$ (open circles). The solid lines denote the best fit predictions of equation (1). See fig. S10 and table S1 for additional data. (b) The average particle velocity parallel to the incline—denoted U_2—increases quadratically with the frequency ω. Markers denote experimental data; solid lines denote the best fit predictions of equation (2). Error bars represent one standard deviation above/below the mean.

that the axis of the rotating field is aligned parallel to the gravity direction; the effect of misalignment is detailed in the Supporting Information.

This model reproduces and explains the observed dynamics of a rotating sphere on an inclined substrate. The migration velocity scales linearly with the incline angle α such that no motion is predicted on a level surface. Particle motion perpendicular to the incline is analogous to that of field-drive "rolling",[35] which is proportional to both the rotation frequency ω and the hydrodynamic traction κ. The traction describes the strength of rotation-translation coupling and can be interpreted as the ratio between the linear and angular velocity of a force-free particle, $\kappa = U_1/a\Omega_2$.[44] In contrast to no-slip frictional rolling ($\kappa = 1$), lubrication theory predicts a maximum traction of $\kappa = 0.25$ for a solid sphere approaching contact with a plane substrate.[43] As a result, the terms of order κ^2 in equations (1) and (2) are often negligible. Particle motion parallel to the incline has two contributions: one due to gravity which is independent of frequency and another due to field-driven rotation which scales as ω^2. This second contribution—termed topotaxis[34]—depends on the parameter λ, which describes the relative resistance of particle rotation about axes parallel and perpendicular to the surface. Here, λ is greater than one, which means that it is easier to rotate a sphere about an axis normal to the surface than about an axis parallel to the surface. As a result, topotaxis in a rotating field is directed up the inline (see also movie S8).

Fitting the dynamical model to the frequency-dependent migration velocity, we obtain good agreement and physically reasonable parameter estimates (Fig. 2, solid curves). The inferred surface separation is 0.36 μm based on the data in Figure 2 for one particle; data for other particles are summarized in Table S1. The magnetic relaxation rate is estimated to be $\omega_0 = 130$ rad/s, which implies a magnetic moment $m = 1.3 \times 10^{-12}$ A m^2. The inferred gravitational parameter is $G = 0.0021$, which implies a density contrast of 17 kg/m^3 between the particle and the solvent. These inferences are largely consistent from particle to particle (see Fig. S10 and Table S1); however, there is variability in the inferred surface separation and thereby the traction κ, which controls the speed of rotation-induced translation. The

surface separation $\delta = 0.1\text{-}1$ μm and its variation may be caused by surface asperities on the Janus spheres that act to lift the particle center as it rotates. Despite some heterogeneity between the particles, the frequency-dependent dynamics of each individual particle on the inclined surface is well described by the dynamical model.

Toggled fields isolate non-reciprocal contributions to particle motion

At sufficiently low frequencies, the model predicts that the particle's magnetic moment will rotate in lock-step with the external field. When the surface is inclined, the particle experiences greater resistance to rotation on the uphill side than on the downhill side, resulting in particle translation perpendicular to the incline direction. Owing to the kinematic reversibility of low Reynolds hydrodynamics,[45] the particle moves in the opposite direction upon reversing the angular velocity of the rotating field. At higher frequencies, however, the magnetic moment begins to lag behind the driving field as illustrated in Figure 3. As it strives to "catch up" with the rotating field, the particle prefers to rotate about the surface normal vector $\mathbf{n}$ due to the lower hydrodynamic resistance compared to that of directions $\mathbf{t}_x$ and $\mathbf{t}_y$ tangent to the surface. As a result, the magnetic moment $\mathbf{m}$ deviates from the xy-plane of the external field (Fig. 3). Importantly, this out of plane component does not switch direction upon reversing the rotation of the field. Non-reciprocal motion of the particle in the yz plane leads to uphill migration for both positive and negative frequencies (Fig. 3, insets).

Our results indicate that particle motion perpendicular to the incline direction can be eliminated by toggling the direction of the rotating field. By contrast, previous theoretical work used complex time-periodic fields of a single "handedness" to achieve the same end.[34] To prohibit motion on a level substrate, such fields satisfy a symmetry condition whereby rotation of the field about the z-axis by an angle $\varphi_n = 2\pi/n$ is equivalent to a corresponding shift in phase. This condition implies that $R_z(\varphi_n)\mathbf{B}(\omega t) = \mathbf{B}(\omega t \pm \varphi_n)$ where R_z is a coordinate rotation matrix,[46] n is a positive integer, and $\pm$ correspond to "left" and "right"

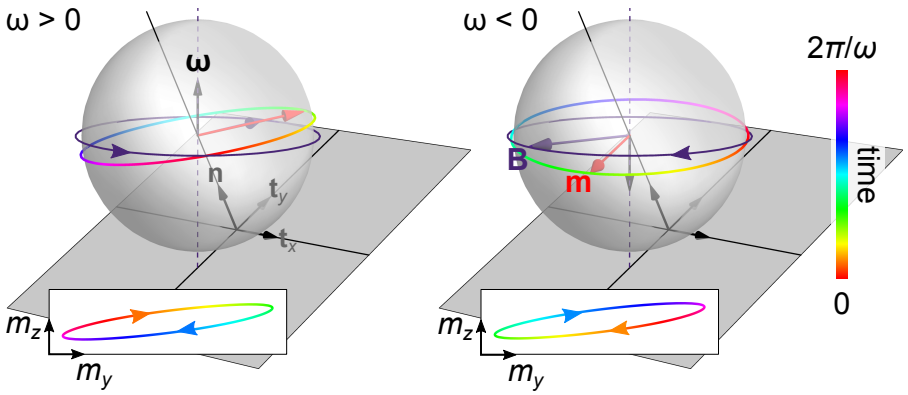

Figure 3: Simulated dynamics of the magnetic moment $\mathbf{m}$ (red vector) illustrates the mechanism of uphill migration for positive (left) and negative (right) frequencies $\boldsymbol{\omega} = \omega \mathbf{e}_z$. The multicolored curve shows the path of the moment during one revolution of the rotating field $\mathbf{B}(t)$ (purple vector). The insets show the projection of the moment's path in the yz plane. See also movie S8.

handed fields, respectively. To eliminate motion perpendicular to the incline, one can design complex fields of a single handedness or simply toggle between right and left handed fields.

Topotaxis directs particle migration on spherical bowls and domes

For curved surface topographies $h(x, y)$ characterized by small inclines ($|\nabla h| \ll 1$) and low curvature ($K \approx \nabla^2 h \ll a^{-1}$), we hypothesized that field-driven particle motions would be well described by the predictions above for inclined planes. To test this hypothesis, we quantify the motion of magnetic spheres moving on spherical bowls and domes in a rotating magnetic field (Fig. 4; Movies S2 and S3). These circular features—obtained from microlens arrays—have a diameter of 180 μm, height / depth of 22 μm, and mean curvature of $K = 0.0052$ μm^{-1} as confirmed by profilometry (Fig. S8). Owing to their axial symmetry, it is not necessary to toggle the frequency of the rotating field to demonstrate uphill migration to the bowl's edge or the dome's crest. Instead, we apply a constant angular frequency in the z-direction ($\omega > 0$), which drives particle motion along spiral trajectories about the center of the bowl or dome.

On the concave bowl ($K > 0$), particles move along anticlockwise spirals when viewed from below (Fig. 4a). At low frequencies, the particle spirals inward to the center of the

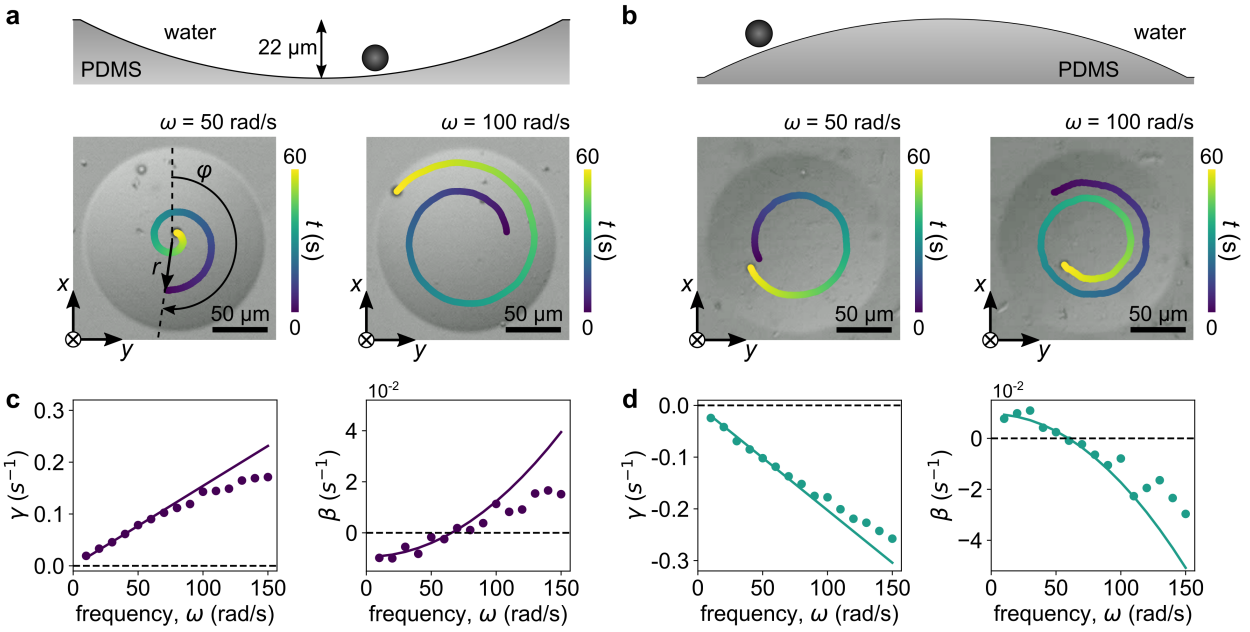

Figure 4: Individual particles moving on bowl- and dome-shaped landscapes. (a) Schematic illustration of a spherical bowl of radius $R = 90$ μm and depth $d = 22$ μm; the 10 μm sphere is drawn to scale. A rotating magnetic field with frequency $\omega = 50$ rad/s leads the particle to spiral inward toward the bottom of the bowl (left). The phase φ and radius r of the particle position at time $t = 0$ s are denoted in the figure. A higher frequency $\omega = 100$ rad/s leads the particle to spiral out of the well against the force of gravity (right). (b) Schematic illustration of a spherical dome of radius $R = 90$ μm and depth $d = 22$ μm. A rotating magnetic field with frequency $\omega = 50$ rad/s leads the particle to spiral down the side of the dome (left). A higher frequency $\omega = 100$ rad/s leads the particle to spiral inward to the dome's crest against the force of gravity (right). (c) For the bowl ($K > 0$), the rate of angular motion γ increases linearly with the frequency ω of the rotating field (left); the rate of radial motion β increases quadratically with ω (right). (d) For the dome ($K < 0$), γ decreases linearly with the frequency ω and β decreases quadratically with ω.

bowl; at sufficiently high frequencies, the particle spirals outward to the edge of the bowl. Upon exiting the bowl onto a level plateau, its field-driven migration ceases. On the convex dome ($K < 0$), particles move in the opposite direction along clockwise spirals when viewed from below (Fig. 4b). The particle spirals outward to the edge of the dome at low frequencies and inward to the crest of the dome at high frequencies. Consistent with predictions of the dynamical model, these trajectories are well described by the following expressions for the radial and angular coordinates of the particle (Fig. 4a; see also Fig. S5)

$$r(t) = r_0 e^{\beta t} \quad \text{and} \quad \varphi(t) = \varphi_0 - \gamma t \tag{3}$$

Here, r_0 and φ_0 denote the initial radial and angular position of the particle at time $t = 0$; β and γ are frequency-dependent rate parameters that describe particle motion in the radial and angular directions.

As detailed in the Supporting Information, the rate parameters γ and β describing motion perpendicular and parallel to the to the local incline are closely related to the velocity components U_1 and U_2 of equations (1) and (2). From the particle trajectories, we infer the values of γ and β for a series of different rotation frequencies (Figs. 4c,d). Consistent with model predictions, the rate parameter γ describing motion perpendicular to the incline varies linearly with frequency with the sign determined by that of the mean curvature (cf. left panels of Fig. 4c and 4d) and the angular frequency (not shown). By contrast, the rate parameter β describing motion parallel to the incline varies quadratically with frequency with the sign determined by the mean curvature (cf. right panels of Fig. 4c and 4d). Moreover, by fitting the rate parameters γ and β against model predictions, the inferred estimates for the relaxation frequency ω_0, gravity parameter G, and surface separation agree with those obtained from data on the flat inclines (see Table S2 and Figs. S11 and S12 for additional data).

Topotaxis directs self-guided navigation of multiple particles in a common field

Finally, we demonstrate the unique capability of topotaxis to direct the simultaneous migration of multiple independent particles along different directions as determined by the local surface topography. We identify four particles in neighboring bowls and apply a common rotating field to drive uphill migration (Fig. 5a and movie S4). The particles trace distinct spiral trajectories out of their respective bowls with differences attributed to the different surface separations for each particle. Alternatively, when the same particles are energized by a toggled rotating field, they migrate out of the bowl along different directions determined by their initial positions (Fig. 5b and movie S5). Likewise, two particles on neighboring dome-shaped landscapes climb their respective hills along spiral trajectories of opposite handedness than observed for the domes (Fig. 5c and movie S6). When those particles are initialized on opposite sides of their respective domes, the toggled field drives uphill migration along opposite directions in a common field (Fig. 5d and movie S7).

The dynamics of neighboring particles are expected to influence one another by magnetic and hydrodynamic interactions; however, these effects are small when particles are separated by several particle diameters. For spheres rotating about an axis normal to a plane wall, both hydrodynamic and magnetic interactions scale inversely with particle separation as r^{-4} (see Supporting Information). The ratio of these interactions is proportional to the dimensionless Mason number $\mathrm{Ma} = 72\eta\omega V_\mathrm{p}^2/\mu_0 m^2$, where $V_\mathrm{p} = 4\pi a^3/3$ is the particle volume and μ_0 is the vacuum permeability.[9,47] For rotation frequencies equal to the relaxation rate $\omega = \omega_0$, the Mason number for these particles is of order unity, indicating that hydrodynamic and magnetic interactions are of similar magnitude. Comparing the speed of topotaxis to that of dipole-dipole attraction, the latter is negligible for particle separations $r \gg 4a$. A similar condition is obtained by comparing the speed of topotaxis to that due to hydrodynamic interactions between the particles (see Supporting Information).

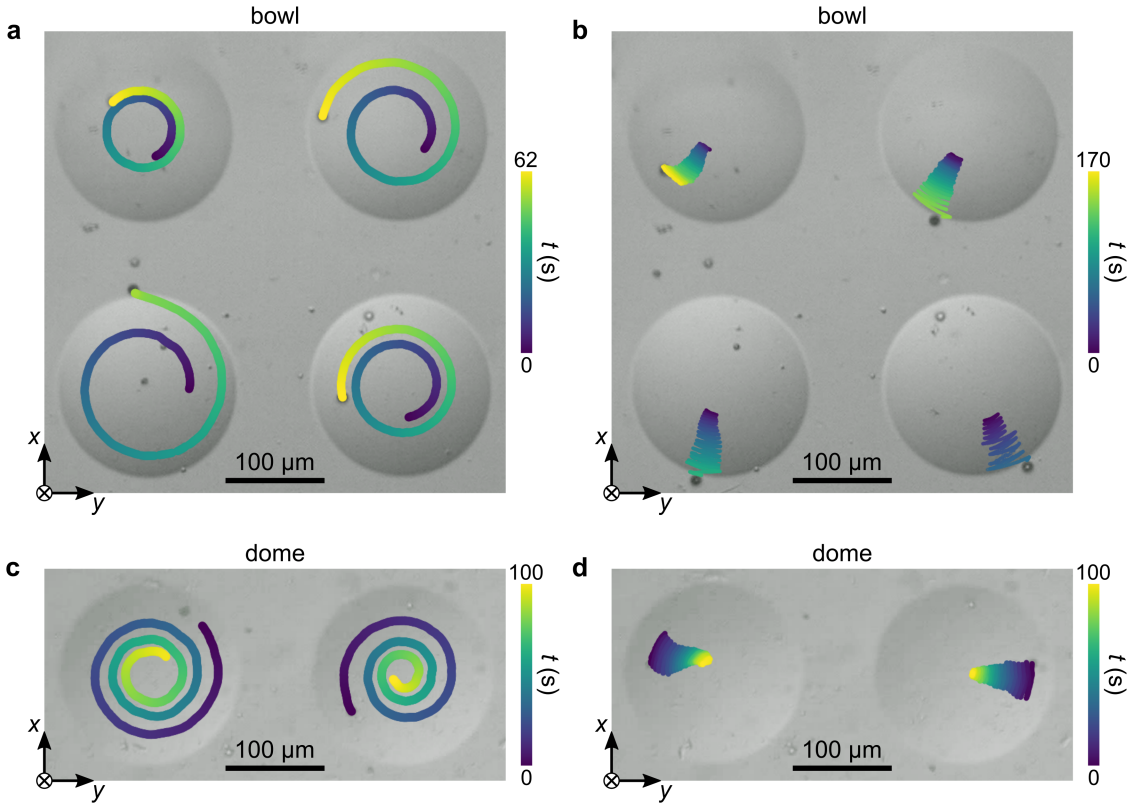

Figure 5: Multiple particles moving in a common field on arrays of bowls and domes. (a) Four particles moving on neighboring bowls spiral outward under the influence of a rotating field with constant frequency $\omega = 120$ rad/s. (b) The same particles Uphill motion is also observed for all particles in bowls under zig-zag field with frequency $\omega = 100$ rad/s. (c) Particles on the dome surface generate uphill motion with singular rotation field with frequency $\omega = 100$ rad/s and (d) zig-zag field with frequency $\omega = 100$ rad/s

Conclusion

We demonstrate that a simple rotating field can drive the migration of magnetic spheres up an inclined substrate. This motion is well described by a dynamical model based on magnetic actuation and low-Reynolds number hydrodynamics for the sphere-plane geometry. Using the model, the waveform of the driving field can be further designed to enhance the speed of topotaxis or change its direction. In the absence of gravity, the migration speed along the inclined direction has the form $\langle U_2 \rangle = C\kappa a \alpha k^2/\omega_0$, where C is a dimensionless constant, and k is a characteristic rate of the driving field (see Supporting Information). For the simple rotating field, this rate is identical to the frequency ($k = \omega$); however, this need not be the case for complex time-periodic fields where $k \gg \omega$. The constant C depends on the waveform of the driving field and the parameter λ that describes the asymmetry between rotation about axes parallel and perpendicular to the surface. For $\lambda = 1.87$ (i.e., a surface separation of $0.01a$), the rotating field is characterized by $C = 0.35$ as compared to $C = 1.31$ for more complex fields optimized to enhance topotaxis.[34] In principle, other driving fields can be used to enhance particle migration down the inclined substrate if desired.[34]

The self-guided navigation of multiple independent particles on topographic landscapes may be useful for microrobotics, distributed sensing, and particle separations. Topotaxis is "self-guided" in the sense that the direction and speed of particle motion is determined not by the global magnetic field but rather by the local particle environment—namely, the surface topography. As a result, a common driving field can be used to power and direct the uphill migration of multiple independent particles—even with little or no information about the particle positions and the surface topography. The capacity for self-guided navigation despite global actuation and limited information is potentially useful for designing and deploying magnetic microrobots with increasing levels of autonomy. Depending on the driving field, such particles could be instructed to move to local maxima or to trace contour lines of the surface topography along clockwise or anticlockwise paths. Moreover, by modulating the field between hill climbing, contour tracing, and hill descending modalities, one could

bias particle migration towards global maxima (or minima) of a given surface. Finally, the sensitivity of topotaxis to particle properties such as size, magnetic moment, and surface separation could also provide a basis for particle characterization and separations.

Future efforts to understand and control self-guided microrobots in time-varying magnetic fields should investigate the influence of particle shape, generalize topotaxis to other gradients, and explore extensions in three dimensions (3D). The present study uses spherical particles on long wavelength topographies due to the simplicity of the sphere-plane geometry, for which the hydrodynamic mobility tensor can be easily evaluated. The speed of topotaxis, however, would likely be enhanced for anisotropic particles (e.g., ellipsoids[48]) that exhibit stronger coupling between particle rotation and translation near a surface. In addition to particle shape, further work is needed to explore the influence of "rough" topographies with particle-scale features.[49] More generally, self-guided particle motion encoded by time-varying fields should be feasible in gradients of other physical quantities that influence the particle dynamics (e.g., fluid viscosity, shear flow). The ability to navigate shear fields in fluidic networks would be particularly useful in creating microrobots for biomedical applications within the human vasculature. Realizing such applications, however, would require a conceptual shift from the 2D motions described here to those in 3D. In 2D, the rotational symmetry of the driving field prohibits motion in the absence of a gradient (e.g., on a level surface); no analogous design principle has been identified for 3D motion. Additionally, self-guided navigation through complex fluids such as blood may require new designs for the driving field and the particle shape that account for the frequency-dependent, non-Newtonian rheology of the medium. Despite these challenges, we remain optimistic that time-varying magnetic fields can be programmed to create self-guided microrobots capable of sensing asymmetries in their local environment and responding with desired behaviors.[35]

Methods

Fabrication of magnetic Janus spheres

Magnetic Janus particles were prepared by spin-coating polystyrene (PS) spheres onto a silicon wafer and depositing a nickel layer onto the spheres by e-beam evaporation. Fluorescent PS spheres (ThermoFisher, 10 μm diameter) were dispersed in methanol at a concentration of 0.5 wt% and sonicated for 1 min to disrupt any aggregates. Silicon wafers (Virginia Semiconductor, Inc.) were cleaned by immersion in acetone for 10 min followed by methanol for 5 min, rinsed with deionized water, and dried with nitrogen. 0.8 mL of the particle suspension was deposited onto the silicon wafer using a spin coater at 800 rpm for 70 s. The particle-coated silicon wafer was then transferred to a cleanroom facility for electron beam evaporation to deposit material layers onto the particles. Three layers—a 5 nm titanium adhesion layer, a 40 nm magnetic nickel layer, and a 20 nm passivating layer of silicon dioxide—were deposited sequentially onto the exposed hemispheres of the particles using an Angstrom EvoVac deposition system. The magnetic Janus particles were collected from the silicon wafer using a soft nylon hair brush (UPINS, 7mm hair width, 12mm hair length) and dispersed in an aqueous solution of 0.5% Tween-20 for use.

Fabrication of PDMS landscapes

Polydimethylsiloxane (PDMS) landscapes with bowl-shaped impressions were fabricated by soft lithography[50] using a microlens array as a template. The PDMS base and curing agent (Dow Sylgard 184 Silicone Elastomer) were mixed in a 7:1 ratio (28 g base, 4 g curing agent) and stirred for 10 minutes. The mixture was then placed in a desiccator and degassed for 5 minutes to remove air bubbles. The fused silica microlens array (Edmund Optics) was placed in a petri dish with the lens side facing up. The degassed PDMS mixture was carefully poured over the template and allowed to rest at room temperature for 1 hour in the desiccator to remove any remaining bubbles. The petri dish containing the PDMS and the lens array was

placed in an oven preheated to 60°C and cured for 2 hours. The cured PDMS was carefully peeled away from the template to yield the bowl-shaped landscape. PDMS landscapes with dome-shaped features were fabricated in similar fashion using the previously prepared PDMS mold with bowl-shaped impressions as a master. To prevent adhesion between the PDMS master and the PDMS replica, a solution of Tween 20 (10 wt%) dissolved in 75% ethanol was applied to the surface of the PDMS master and dried for 30 minutes at room temperature prior to use.[51]

Topotaxis experiments

The dilute dispersion of magnetic Janus particles was enclosed in a glass chamber, subject to a rotating magnetic field, and imaged by optical microscopy. Approximately 10 μL of the particle dispersion was sealed between a glass slide and a cover slip using a Gene Frame (Fisher Scientific). Prior to assembly, the glass slide was treated with an atmospheric plasma for 15 minutes to prevent particle adhesion onto the glass surface. The glass chamber was positioned above an inverted microscope (Nikon Eclipse TI-U) and imaged under brightfield using 4X objective. The orientation of the chamber was controlled by four adjustable screws positioned below each corner of its base. The chamber was surrounded by six coils of a custom triaxial electromagnet (Stangenes Industries Inc.) calibrated by magnetic field sensor (Ametes MFS3A). The computed controlled coils supplied a rotating magnetic field of various frequencies with a constant magnitude of 0.5 mT. The spatial homogeneity of the applied field was characterized within the 13 mm × 10 mm field of view of the imaging plane; variations were less than 0.5% as shown in Fig. S9. Videos of field-driven particle motion were captured at 10 frames per second by a digital camera (The Imaging Source, DFK 33UP2000).

Model of field-driven particle dynamics

We consider a magnetic sphere with radius a and permanent magnetic moment $\mathbf{m}$ moving through a viscous fluid at a fixed height above a solid plane under the influence of a time-

varying magnetic field $\mathbf{B}(t)$. In a uniform field, the particle experiences a magnetic torque, $\mathbf{T}_\mathrm{m} = \mathbf{m} \times \mathbf{B}(t)$, but no magnetic force, $\mathbf{F}_\mathrm{m} = 0$. The gravitational force on the particle is $\mathbf{F}_\mathrm{g} = M\mathbf{g}$ where M is the bouyant mass of the particle, and $\mathbf{g}$ is the acceleration due to gravity. Approximating the Janus particle as a homogeneous sphere, there is no gravitational torque, $\mathbf{T}_\mathrm{g} = 0$. Additionally, we assume that the surface exerts a force $\mathbf{F}_\mathrm{s}$ on the particle as to maintain a constant surface separation δ, which is small compared to the size of the particle ($\delta \ll a$). In the absence of inertial effects (i.e., at low Reynolds number), the external forces and torques on the particle are balanced by the hydrodynamic force and torque, which are related to the particle's linear velocity $\mathbf{U}$ and angular velocity $\mathbf{\Omega}$ as

$$\begin{pmatrix} \mathbf{U} \\ \mathbf{\Omega} \end{pmatrix} = \begin{pmatrix} \mathbf{a} & \tilde{\mathbf{b}} \\ \mathbf{b} & \mathbf{c} \end{pmatrix} \cdot \begin{pmatrix} \mathbf{F}_\mathrm{g} + \mathbf{F}_\mathrm{s} \\ \mathbf{T}_\mathrm{m} \end{pmatrix} \tag{4}$$

where $\mathbf{a}$, $\mathbf{b}$, $\tilde{\mathbf{b}}$, $\mathbf{c}$ are components of the hydrodynamic mobility tensor. For a sphere above a plane, the mobility tensors have the form

$$\begin{aligned} \mathbf{a} &= \frac{1}{6\pi\eta a}\left[Y_a(\boldsymbol{\delta} - \mathbf{nn}) + X_a\,\mathbf{nn}\right] \\ -\mathbf{b} = \tilde{\mathbf{b}} &= \frac{1}{6\pi\eta a^2} Y_b\,\boldsymbol{\epsilon}\cdot\mathbf{n} \\ \mathbf{c} &= \frac{1}{6\pi\eta a^3}\left[Y_c(\boldsymbol{\delta} - \mathbf{nn}) + X_c\,\mathbf{nn}\right] \end{aligned} \tag{5}$$

where $\boldsymbol{\delta}$ is the identity tensor, $\boldsymbol{\epsilon}$ is the Levi-Civita tensor, $\mathbf{n}$ is the unit normal vector directed out of the plane, and X_a, Y_a, etc. are positive mobility coefficients that depend on the ratio δ/a between the surface separation and the sphere radius (see Fig. S1). Together with the kinematics of rigid body motion, equations (4) and (5) describe the dynamics of particle rotation and translation for any field $\mathbf{B}(t)$ and gravity direction $\mathbf{g}$.

As illustrated in Fig. 1a, we consider particle motion along an inclined plane with $\mathbf{n} = -\sin\alpha\mathbf{e}_y + \cos\alpha\mathbf{e}_z$ under the influence a rotating field with angular frequency $\boldsymbol{\omega} = \omega\mathbf{e}_z$ and gravity with acceleration $\mathbf{g} = -g\mathbf{e}_z$. Following Dou *et al.*,[34] we use multiple scale

perturbation methods[39] to derive equations (1) and (2) for the average particle velocity in the limit of small inclines $\alpha \ll 1$ and low frequencies $\omega \ll \omega_0 = mBY_c/6\pi\eta a^3$. Further details of the model and the effects of misalignment between the rotation frequency $\boldsymbol{\omega}$ and the gravity direction $\mathbf{g}$ are provided in the Supporting Information.

The dynamical model neglects contributions due to Brownian motion and surface roughness. Brownian motion is negligible when the rotational diffusivity of the particle is much slower than its field driven rotation—that is, when $D_\mathrm{r} = Y_c k_\mathrm{B}T/6\pi\eta a^3 \ll \omega$. Assuming $\omega \approx \omega_0$, the condition to neglect Brownian motion becomes $mB/k_\mathrm{B}T \gg 1$, where $mB/k_\mathrm{B}T \approx 40,000$ for the present experiments. Though neglected by the model, surface roughness on the particle and/or the substrate can potentially influence the mobility ratios κ and λ that contribute to the speed of topotaxis. For example, frictional contacts between gear-like surface asperities could increase the traction κ by as much as an order of magnitude from $\sim$0.1 to 1 in the no-slip limit.

Data analysis

Brightfield microscopy videos were analyzed using Trackpy[52] (v0.6.2) to locate particles and link their trajectories. For each particle, we obtained a sequence of particle positions $\{x_k, y_k\}$ at regular time intervals $t_k = k\Delta t$ for $k = 0, 1, 2, \ldots$ and $\Delta t = 0.1$ ms. From these data, we used linear regression to infer the x and y components of the particle velocity for each frequency ω and incline angle α. These data are related to the model predictions of equations (1) and (2) by a coordinate rotation that accounts for the small misalignment between the gravity direction and the axis of the rotating field. We used nonlinear regression to infer model parameters—namely, the magnetic relaxation rate ω_0, the surface separation δ/a, the dimensionless gravity parameter G—and two angles characterizing the alignment of the rotating field (see Supporting Information for details).

Acknowledgement

This material is based upon work supported by the National Science Foundation under Grant No. CBET-2153202.

Supporting Information Available

(1) Additional derivations for the dynamics of a field-driven sphere on an inclined plane. (2) Additional details on the analysis of particle tracking data. (3) Comparison of predicted topotaxis in different driving fields. (4) Measured topographies of the PDMS bowls and domes. (5) Measured field strength across the imaging region. (6) Additional data of zig-zag trajectories on inclined planes. (7) Additional data of spiral trajectories on bowls and domes.

References

(1) Dou, Y.; Dhatt-Gauthier, K.; Bishop, K. J. M. Thermodynamic costs of dynamic function in active soft matter. *Curr. Opin. Solid State Mater. Sci.* **2019**, *23*, 28–40.

(2) Zhou, H.; Mayorga-Martinez, C. C.; Pané, S.; Zhang, L.; Pumera, M. Magnetically driven micro and nanorobots. *Chem. Rev.* **2021**, *121*, 4999–5041.

(3) Dreyfus, R.; Baudry, J.; Roper, M. L.; Fermigier, M.; Stone, H. A.; Bibette, J. Microscopic artificial swimmers. *Nature* **2005**, *437*, 862–865.

(4) Zhang, L.; Abbott, J. J.; Dong, L.; Kratochvil, B. E.; Bell, D.; Nelson, B. J. Artificial bacterial flagella: Fabrication and magnetic control. *Appl. Phys. Lett.* **2009**, *94*, 064107.

(5) Ghosh, A.; Fischer, P. Controlled propulsion of artificial magnetic nanostructured propellers. *Nano Lett.* **2009**, *9*, 2243–2245.

(6) Bachmann, F.; Bente, K.; Codutti, A.; Faivre, D. Using shape diversity on the way to structure-function designs for magnetic micropropellers. *Phys. Rev. Appl.* **2019**, *11*, 034039.

(7) Tierno, P.; Golestanian, R.; Pagonabarraga, I.; Sagués, F. Controlled swimming in confined fluids of magnetically actuated colloidal rotors. *Phys. Rev. Lett.* **2008**, *101*, 218304.

(8) Tasci, T. O.; Herson, P. S.; Neeves, K. B.; Marr, D. W. M. Surface-enabled propulsion and control of colloidal microwheels. *Nat. Commun.* **2016**, *7*, 10225.

(9) Driscoll, M.; Delmotte, B.; Youssef, M.; Sacanna, S.; Donev, A.; Chaikin, P. Unstable fronts and motile structures formed by microrollers. *Nat. Phys.* **2017**, *13*, 375–379.

(10) Martinez-Pedrero, F.; Tierno, P. Magnetic propulsion of self-assembled colloidal carpets: efficient cargo transport via a conveyor-belt effect. *Phys. Rev. Appl.* **2015**, *3*, 051003.

(11) Yang, T.; Tasci, T. O.; Neeves, K. B.; Wu, N.; Marr, D. W. M. Magnetic microlassos for reversible cargo capture, transport, and release. *Langmuir* **2017**, *33*, 5932–5937.

(12) Han, K.; Shields IV, C. W.; Diwakar, N. M.; Bharti, B.; López, G. P.; Velev, O. D. Sequence-encoded colloidal origami and microbot assemblies from patchy magnetic cubes. *Sci. Adv.* **2017**, *3*, e1701108.

(13) Tasci, T. O.; Disharoon, D.; Schoeman, R. M.; Rana, K.; Herson, P. S.; Marr, D. W. M.; Neeves, K. B. Enhanced fibrinolysis with magnetically powered colloidal microwheels. *Small* **2017**, *13*, 1700954.

(14) Leclerc, J.; Zhao, H.; Bao, D.; Becker, A. T. In vitro design investigation of a rotating helical magnetic swimmer for combined 3-D navigation and blood clot removal. *IEEE Trans. Robot.* **2020**, *36*, 975–982.

(15) Wang, Q.; Du, X.; Jin, D.; Zhang, L. Real-time ultrasound doppler tracking and autonomous navigation of a miniature helical robot for accelerating thrombolysis in dynamic blood flow. *ACS Nano* **2022**, *16*, 604–616.

(16) Xie, H.; Sun, M.; Fan, X.; Lin, Z.; Chen, W.; Wang, L.; Dong, L.; He, Q. Reconfigurable magnetic microrobot swarm: Multimode transformation, locomotion, and manipulation. *Sci. Robot.* **2019**, *4*, eaav8006.

(17) Yigit, B.; Alapan, Y.; Sitti, M. Programmable collective behavior in dynamically self-assembled mobile microrobotic swarms. *Adv. Sci.* **2019**, *6*, 1801837.

(18) Lobmeyer, D. M.; Biswal, S. L. Grain boundary dynamics driven by magnetically induced circulation at the void interface of 2D colloidal crystals. *Sci. Adv.* **2022**, *8*, eabn5715.

(19) Nelson, B. J.; Kaliakatsos, I. K.; Abbott, J. J. Microrobots for minimally invasive medicine. *Annu. Rev. Biomed. Eng.* **2010**, *12*, 55–85.

(20) Wang, Q.; Chan, K. F.; Schweizer, K.; Du, X.; Jin, D.; Yu, S. C. H.; Nelson, B. J.; Zhang, L. Ultrasound Doppler-guided real-time navigation of a magnetic microswarm for active endovascular delivery. *Sci. Adv.* **2021**, *7*, eabe5914.

(21) Law, J.; Wang, X.; Luo, M.; Xin, L.; Du, X.; Dou, W.; Wang, T.; Shan, G.; Wang, Y.; Song, P.; Huang, X.; Yu, J.; Sun, Y. Microrobotic swarms for selective embolization. *Sci. Adv.* **2022**, *8*, eabm5752.

(22) Sun, M.; Chan, K. F.; Zhang, Z.; Wang, L.; Wang, Q.; Yang, S.; Chan, S. M.; Chiu, P. W. Y.; Sung, J. J. Y.; Zhang, L. Magnetic microswarm and fluoroscopy-guided platform for biofilm eradication in biliary stents. *Adv. Mater.* **2022**, *34*, 2201888.

(23) Lee, J. G.; Raj, R. R.; Day, N. B.; Shields IV, C. W. Microrobots for biomedicine:

unsolved challenges and opportunities for translation. *ACS Nano* **2023**, *17*, 14196–14204.

(24) Jiang, J.; Yang, Z.; Ferreira, A.; Zhang, L. Control and autonomy of microrobots: Recent progress and perspective. *Adv. Intell. Syst.* **2022**, *4*, 2100279.

(25) Wrede, P.; Degtyaruk, O.; Kalva, S. K.; Deán-Ben, X. L.; Bozuyuk, U.; Aghakhani, A.; Akolpoglu, B.; Sitti, M.; Razansky, D. Real-time 3D optoacoustic tracking of cell-sized magnetic microrobots circulating in the mouse brain vasculature. *Sci. Adv.* **2022**, *8*, eabm9132.

(26) Kummer, M. P.; Abbott, J. J.; Kratochvil, B. E.; Borer, R.; Sengul, A.; Nelson, B. J. OctoMag: An electromagnetic system for 5-DOF wireless micromanipulation. *IEEE Trans. Robot.* **2010**, *26*, 1006–1017.

(27) Bishop, K. J. M.; Biswal, S. L.; Bharti, B. Active colloids as models, materials, and machines. *Annu. Rev. Chem. Biomol. Eng.* **2023**, *14*, 1–30.

(28) Hong, Y.; Blackman, N. M.; Kopp, N. D.; Sen, A.; Velegol, D. Chemotaxis of nonbiological colloidal rods. *Phys. Rev. Lett.* **2007**, *99*, 178103.

(29) Dou, Y.; Bishop, K. J. M. Autonomous navigation of shape-shifting microswimmers. *Phys. Rev. Res.* **2019**, *1*, 032030.

(30) Palacci, J.; Sacanna, S.; Abramian, A.; Barral, J.; Hanson, K.; Grosberg, A. Y.; Pine, D. J.; Chaikin, P. M. Artificial rheotaxis. *Sci. Adv.* **2015**, *1*, e1400214.

(31) Ren, L.; Zhou, D.; Mao, Z.; Xu, P.; Huang, T. J.; Mallouk, T. E. Rheotaxis of bimetallic micromotors driven by chemical–acoustic hybrid power. *ACS Nano* **2017**, *11*, 10591–10598.

(32) Lozano, C.; Ten Hagen, B.; Löwen, H.; Bechinger, C. Phototaxis of synthetic microswimmers in optical landscapes. *Nat. Commun.* **2016**, *7*, 12828.

(33) Dai, B.; Wang, J.; Xiong, Z.; Zhan, X.; Dai, W.; Li, C.-C.; Feng, S.-P.; Tang, J. Programmable artificial phototactic microswimmer. *Nat. Nanotechnol.* **2016**, *11*, 1087–1092.

(34) Dou, Y.; Tzelios, P. M.; Livitz, D.; Bishop, K. J. M. Programmable topotaxis of magnetic rollers in time-varying fields. *Soft Matter* **2021**, *17*, 1538–1547.

(35) Dhatt-Gauthier, K.; Livitz, D.; Wu, Y.; Bishop, K. J. M. Accelerating the Design of Self-Guided Microrobots in Time-Varying Magnetic Fields. *JACS Au* **2023**, *3*, 611–627.

(36) Fei, W.; Driscoll, M. M.; Chaikin, P. M.; Bishop, K. J. M. Magneto-capillary dynamics of amphiphilic Janus particles at curved liquid interfaces. *Soft Matter* **2018**, *14*, 4661–4665.

(37) Fei, W.; Tzelios, P. M.; Bishop, K. J. M. Magneto-capillary particle dynamics at curved interfaces: Time-varying fields and drop mixing. *Langmuir* **2020**,

(38) Livitz, D.; Dhatt-Gauthier, K.; Bishop, K. J. M. Magneto-capillary particle dynamics at curved interfaces: inference and criticism of dynamical models. *Soft Matter* **2023**, *19*, 9017–9026.

(39) Strogatz, S. H. *Nonlinear dynamics and chaos: with applications to physics, biology, chemistry, and engineering*; CRC press, 2018.

(40) O'Neill, M. E. A slow motion of viscous liquid caused by a slowly moving solid sphere. *Mathematika* **1964**, *11*, 67–74.

(41) Dean, W.; O'Neill, M. A slow motion of viscous liquid caused by the rotation of a solid sphere. *Mathematika* **1963**, *10*, 13–24.

(42) Jeffery, G. B. On the steady rotation of a solid of revolution in a viscous fluid. *Proc. London Math. Soc.* **1915**, *2*, 327–338.

(43) Goldman, A. J.; Cox, R. G.; Brenner, H. Slow viscous motion of a sphere parallel to a plane wall—I Motion through a quiescent fluid. *Chem. Eng. Sci.* **1967**, *22*, 637–651.

(44) Gao, Y.; Sprinkle, B.; Springer, E.; Marr, D. W.; Wu, N. Rolling of soft microbots with tunable traction. *Sci. Adv.* **2023**, *9*, eadg0919.

(45) Lauga, E.; Powers, T. R. The hydrodynamics of swimming microorganisms. *Rep. Prog. Phys.* **2009**, *72*, 096601.

(46) Diebel, J. Representing attitude: Euler angles, unit quaternions, and rotation vectors. *Matrix* **2006**, *58*, 1–35.

(47) Du, D.; Hilou, E.; Biswal, S. L. Modified Mason number for charged paramagnetic colloidal suspensions. *Phys. Rev. E* **2016**, *93*, 062603.

(48) Lee, J. G.; Al Harraq, A.; Bishop, K. J. M.; Bharti, B. Fabrication and electric field-driven active propulsion of patchy microellipsoids. *J. Phys. Chem. B* **2021**, *125*, 4232–4240.

(49) Yang, T.; Tomaka, A.; Tasci, T. O.; Neeves, K. B.; Wu, N.; Marr, D. W. M. Microwheels on microroads: Enhanced translation on topographic surfaces. *Sci. Robot.* **2019**, *4*, eaaw9525.

(50) Xia, Y.; Whitesides, G. M. Soft lithography. *Annu. Rev. Mater. Sci.* **1998**, *28*, 153–184.

(51) Yang, C.; Wang, W.; Li, Z. Optimization of corona-triggered PDMS-PDMS bonding method. 2009 4th IEEE International Conference on Nano/Micro Engineered and Molecular Systems. 2009; pp 319–322.

(52) Allan, D. B.; Caswell, T.; Keim, N. C.; van der Wel, C. M.; Verweij, R. W. Trackpy: Fast, flexible particle-tracking toolkit. **2024**, 10.5281/zenodo.10696534.

TOC Graphic

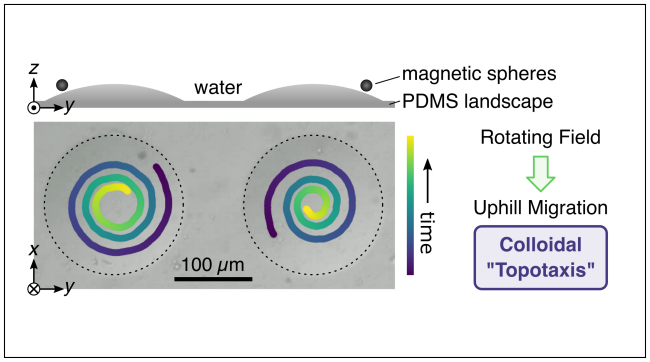
z
y
water
magnetic spheres
PDMS landscape
Rotating Field
Uphill Migration
Colloidal
"Topotaxis"
time
x
y
100 μm